Generally Curved Magnetic Flux Rope Structures

Andreas J. Weiss,[1,2] Teresa Nieves-Chinchilla,[3,4] Christian Möstl,[1] Martin A. Reiss,[1] Tanja Amerstorfer,[1] and Rachel L. Bailey[5]

[1]*Space Research Institute, Austrian Academy of Sciences, Schmiedlstraße 6, 8042 Graz, Austria*
[2]*Institute of Physics, University of Graz, Universitätsplatz 5, 8010 Graz, Austria*
[3]*Heliospheric Physics Laboratory, NASA Goddard Space Flight Center, Greenbelt, MD 20771, USA*
[4]*Department of Physics, Catholic University of America, Washington, DC, USA*
[5]*Zentralanstalt für Meteorologie und Geodynamik, Hohe Warte 38, 1190 Vienna, Austria*

ABSTRACT

We present a new analytical approach with the aim to describe generally curved and twisted magnetic flux rope structures, that are embedded within interplanetary coronal mass ejections, under the constraint of invariant axial flux. In this paper we showcase the simplest case of a generally curved flux rope with a circular cross-section which can be described in terms of the curvature and the torsion of the Frenet-Serret equations. The magnetic field configuration, for the axial and poloidal field components, are described in terms of a radial expansion using a Legendre basis. We further derive equations that allow us to configure our model for any arbitrary magnetic twist and also evaluate the force distribution. We show the effects and differences of our proposed model compared to a purely cylindrical or toroidal geometry using an arbitrarily twisted exemplary flux rope structure with an uniformly twisted magnetic field configuration. In order to indirectly compare our model with real in-situ measurements we generate two synthetic in-situ profiles using virtual spacecraft trajectories, realistically simulating apex and flank encounters of an interplanetary coronal mass ejection. This proposed model presents an intermediate steps towards describing more complex flux rope structures with arbitrary cross-section shapes.

1. INTRODUCTION

A magnetic flux rope is a confined magnetic field structure consisting of a flux tube and an axially twisted magnetic field. These structures play a prominent role in heliophysics and in many other astrophysical settings, and are believed to at the center of any interplanetary coronal mass ejection (ICME). The in-situ magnetic field measurements of these flux ropes structures within ICMEs were initially named magnetic clouds (Burlaga et al. 1981) before they were associated with coronal mass ejections (Gosling et al. 1991) and successively found to closely follow the signature of a magnetic flux rope (Lepping et al. 1990; Bothmer & Schwenn 1998).

The basic magnetic field structure of a flux rope can be described using cylindrical analytical models such as uniform-twist force-free models (Gold & Hoyle 1960; Hu et al. 2015) or a linear force-free configurations (Lundquist 1950; Lepping et al. 1990; Farrugia et al. 1995). From in-situ magnetic field measurements and white-light observations using coronagraphs and heliospheric imagers (e.g. Mulligan & Russell 2001; Vandas et al. 2005; Vourlidas et al. 2013; Davies et al. 2021) we know that these cylindrical approximations are highly simplified, and that the geometry of ICMEs can be significantly more complicated due to interaction with the coronal magnetic field (Lugaz et al. 2012; Kay et al. 2015; Möstl et al. 2015) or the solar wind (Riley & Crooker 2004; Liu et al. 2006; Démoulin & Dasso 2009). These general deformations can be very hard to identify in the local in-situ magnetic field measurements. The measurements are also affected by other processes, such as flux rope expansions (Leitner et al. 2007; Gulisano et al. 2012). These problems are additionally exacerbated when only single spacecraft measurements are available.

Recent efforts have focused on constructing models with higher complexity regarding the geometry or the internal magnetic field structure with the aim of better reconstructing the measured in-situ signatures. These studies include purely analytical approaches (Hidalgo et al. 2002; Vandas & Romashets 2017a,b; Nieves-Chinchilla et al. 2018), and also semi-analytical models (Isavnin 2016; Kay & Gopalswamy 2018; Weiss et al. 2021). One of they key components of

Corresponding author: Andreas J. Weiss
andreas.weiss@oeaw.at

any recently developed analytical model is axial invariance so that the basic geometry always corresponds to a cylinder and torus and only the cross-sections are changed. This excludes the possibility of modelling any axial deformations which are expected to appear (e.g. Rollett et al. 2014; Hinterreiter et al. 2021).

In this paper, we use the mathematical framework developed in Nieves-Chinchilla et al. (2016, 2018) (henceforth referred to as NC16/NC18) and introduce a cylindrical flux rope model that includes magnetic fields, but is allowed to possess an arbitrary axial curvature and does not require any axial symmetry. The theoretical magnetic field model is derived in detail in Section 2. Beyond the derivation of a solution for the magnetic field we also attempt to configure our model in terms of an arbitrarily predetermined twist distribution function (2.4). Instead of validating our model with respect to in-situ magnetic field measurements of real ICME's we will only focus on purely synthetic results as we believe that any analysis without considering elliptical or more complicated cross-sections is not of much benefit. An exemplary geometry and related magnetic field solution are shown in Section 3. A discussion of our approach is performed in 4 and we also give an outline of how our model can be extended to a more general case which includes more complicated cross-sections.

2. CURVED FLUX ROPE MODEL

We begin by describing the deformation of our structure via the deformation of the central flux rope axis in terms of an arbitrarily parametrized path $\boldsymbol{\gamma}(s)$. We define the unit length velocity field $\boldsymbol{t}(s) = \partial_s \boldsymbol{\gamma}(s)/\|\partial_s \boldsymbol{\gamma}(s)\|$ and further introduce two additional vector fields $\boldsymbol{u}(s)$ and $\boldsymbol{v}(s)$ so that $\{\boldsymbol{t}(s),\ \boldsymbol{u}(s),\ \boldsymbol{v}(s)\}$ forms a properly orientated orthonormal set of vectors. The properly orientated orthogonality condition is also equivalent to $\boldsymbol{v}(s) = \boldsymbol{t}(s) \times \boldsymbol{u}(s)$ and the two vectors $\{\boldsymbol{u}(s), \boldsymbol{v}(s)\}$ are thus defined up to an arbitrary angle of rotation. This degree of freedom, for the angle of ration, will be irrelevant for our paper as we will only consider a cylindrical cross-section so that the overall geometry is independant of the particular choice for this angle. With the help of these definitions we can set up an appropriate curvilinear coordinate system (r, s, φ) for our curved flux rope geometry:

$$\boldsymbol{r}(r, s, \varphi) = \boldsymbol{\gamma}(s) - r\sigma \cos(\varphi)\boldsymbol{u}(s) - r\sigma \sin(\varphi)\boldsymbol{v}(s), \quad (1)$$

where σ describes the half-width of the flux rope. The flux rope volume is then defined by the coordinate range $r \in [0, 1]$, $s \in [0, s_{\max}]$ and $\varphi \in [0, 2\pi]$. We will generally omit the (r, s, φ) dependence for any quantities or vectors defined within this coordinate system unless required for clarity.

We then attempt to construct the covariant basis vectors of our custom coordinate system which are given as:

$$\left\{\boldsymbol{\epsilon}_r, \boldsymbol{\epsilon}_s, \boldsymbol{\epsilon}_\varphi\right\} = \left\{\frac{\partial \boldsymbol{r}(r, s, \varphi)}{\partial r}, \frac{\partial \boldsymbol{r}(r, s, \varphi)}{\partial s}, \frac{\partial \boldsymbol{r}(r, s, \varphi)}{\partial \varphi}\right\}. \quad (2)$$

In order to compute the axial derivative in Eq. (2) we are further required to use a more specific description for the two vectors $\boldsymbol{u}(s)$ and $\boldsymbol{v}(s)$. In this paper we will focus on an approach using the so-called Frenet-Serret frame which provides a straightforward way to not only compute the axial derivatives but also construct the vectors themselves. It is important to note that this is not the only approach and that the Frenet-Serret frame has significant issues in implementation for many scenarios (e.g. Bishop 1975).

As in NC18 the basis vectors $\left\{\boldsymbol{\epsilon}_r, \boldsymbol{\epsilon}_s, \boldsymbol{\epsilon}_\varphi\right\}$ will not necessarily be orthonormal. We must distinguish between covariant and contravariant vector quantities and use generalized forms for any vector operations. We will not repeat the required basic definitions as they are explained in detail and used in NC18. We also attempt to use the same conventions in order to reduce any possible confusion. An extensive review can be found in [math reviews]. We make use of standard Einstein notation with summation over double indices, upper and lower indices indicating contravariant and covariant quantities respectively and raising or lowering of indices via contraction with the metric tensor. Any quantities described in our coordinate system with the non unit basis vectors are denoted with a c subscript and related to the scaled physical quantities via the appropriate scale factors.

2.1. *Coordinate System: Frenet-Serret*

A natural set of vectors that can be constructed for any space curve are the so-called Frenet-Serret vectors $\{\boldsymbol{t}(s),\ \boldsymbol{u}(s) = \boldsymbol{n}(s),\ \boldsymbol{v}(s) = \boldsymbol{b}(s)\}$ that are defined as:

$$\boldsymbol{t}(s) = \partial_s \boldsymbol{\gamma}(s)/l(s) , \quad (3)$$

$$\mathbf{n}(s) = \partial_s \boldsymbol{t}(s)/\|\partial_s \boldsymbol{t}(s)\| , \quad (4)$$

$$\boldsymbol{b}(s) = \boldsymbol{t}(s) \times \boldsymbol{n}(s), \quad (5)$$

where we introduce $l(s) = \|\partial_s \boldsymbol{\gamma}(s)\|$ as a shorthand for the arc-length element. This factor is important for calculations within our coordinate system but it must disappear in any physical results as any physical quantities must be independant of the used parametrization for $\boldsymbol{\gamma}(s)$. As a consequence of our definition used in Eq. (1) the angular parameter φ is set so that $\varphi = 0$ corresponds to the most "outer" point of the curved flux rope and $\varphi = \pi$ the most "inner" point. The accompanying Frenet-Serret equations describe the axial evolution of the basis vectors with respect to the axial parameter:

$$\partial_s \boldsymbol{t}(s) = l(s)\kappa(s)\boldsymbol{n}(s), \quad (6)$$

$$\partial_s \boldsymbol{n}(s) = -l(s)\kappa(s)\boldsymbol{t}(s) + l(s)\tau(s)\boldsymbol{b}(s), \quad (7)$$

$$\partial_s \boldsymbol{b}(s) = -l(s)\tau(s)\boldsymbol{n}(s), \quad (8)$$

where $\kappa(s)$ is the curvature and $\tau(s)$ the torsion of the underlying curve. The Frenet-Serret equations allow us to directly compute the non unit coordinate basis vectors from Eq. (2) in terms of the curvature and the torsion so that:

$$\epsilon_r = -\sigma\left[\cos(\varphi)\boldsymbol{n}(s) + \sin(\varphi)\boldsymbol{b}(s)\right], \qquad (9)$$

$$\begin{aligned}\epsilon_s = &\left[1 + r\sigma\kappa(s)\cos(\varphi)\right]l(s)\boldsymbol{t}(s) \\ &+ r\sigma\tau(s)\left[\sin(\varphi)l(s)\boldsymbol{n}(s) - \cos(\varphi)l(s)\boldsymbol{b}(s)\right],\end{aligned} \qquad (10)$$

$$\epsilon_\varphi = r\sigma\left[\sin(\varphi)\boldsymbol{n}(s) - \cos(\varphi)\boldsymbol{b}(s)\right]. \qquad (11)$$

Figure 1 shows an example of a curved flux rope with the Frenet-Serret vectors and the related basis vectors of our curvilinear coordinate system.
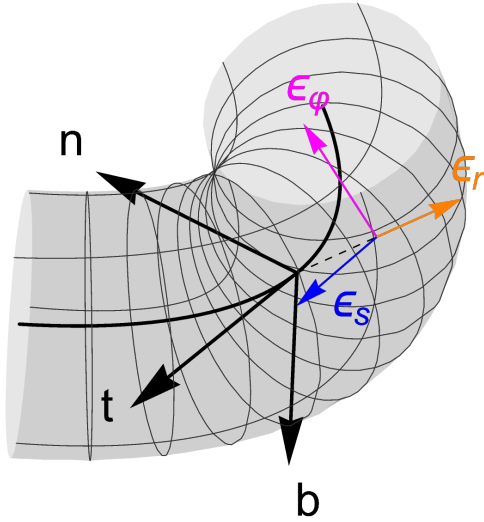

Figure 1. Curved flux rope with the Frenet-Serret vectors $\{\boldsymbol{t}(s), \boldsymbol{n}(s), \boldsymbol{b}(s)\}$ (black) and the corresponding coordinate system basis vectors $\{\epsilon_r, \epsilon_s, \epsilon_\varphi\}$ (orange, blue, magenta) at a random point on the edge ($r = 1$). The coordinate system basis vectors are not shown to scale and have been re-scaled to unity.

Using the expressions for the basis vectors in Eqs. (9-11) we can subsequently construct the covariant metric tensor $g_{ij} = \epsilon_i \cdot \epsilon_j$. The metric tensor entries and the related scale factors are given by:

$$g_{rr} = h_r^2 = \sigma^2, \qquad (12)$$

$$\begin{aligned}g_{ss} = h_s^2 = &\,l^2(s)\left[1 + r\sigma\kappa(s)\cos(\varphi)\right]^2 \\ &+ r^2\sigma^2 l^2(s)\tau^2(s),\end{aligned} \qquad (13)$$

$$g_{\varphi\varphi} = h_\varphi^2 = r^2\sigma^2, \qquad (14)$$

$$g_{rs} = g_{sr} = 0, \qquad (15)$$

$$g_{r\varphi} = g_{\varphi r} = 0, \qquad (16)$$

$$g_{s\varphi} = g_{\varphi s} = r^2\sigma^2 l(s)\tau(s), \qquad (17)$$

where we find that only the $g_{s\varphi}$ off-diagonal component does not vanish. Finally, the metric determinant g is given by:

$$g = r^2\sigma^4 l^2(s)\left[1 + r\sigma\kappa(s)\cos(\varphi)\right]^2. \qquad (18)$$

The Frenet-Serret approach not only provides a straightforward framework for constructing the metric tensor with which we can describe Maxwell's equations within our curved flux rope geometry. It is also the most simple direct implementation as Eqs. (3-5) and Eqs. (9-11) allow us to fully construct the appropriate geometry for any given path $\gamma(s)$. The most significant issue with the Frenet-Serret frame is that it is not defined for points on the curve $\gamma(s)$ where the curvature vanishes as the normal vector $\boldsymbol{n}(s)$ is then ill-defined. As we only consider a circular cross-section with azimuthal symmetry this problematic case is not an issue since the solutions converge to the cylindrical solutions which only depend on the radial distance.

2.2. Magnetic Field Solutions

We now attempt to find a solution for the Maxwell equations in our custom curvilinear coordinate system. As in NC16/NC18, we implicitly assume that the contravariant radial magnetic field component B_c^r vanishes. The Maxwell equations then take the form:

$$0 = \partial_s\left(\sqrt{g}B_c^s\right) + \partial_\varphi\left(\sqrt{g}B_c^\varphi\right), \qquad (19)$$

$$\mu_0 j_c^r = \frac{1}{\sqrt{g}}\left[\partial_s\left(g_{s\varphi}B_c^s + g_{\varphi\varphi}B_c^\varphi\right) - \partial_\varphi\left(g_{ss}B_c^s + g_{s\varphi}B_c^\varphi\right)\right], \qquad (20)$$

$$\mu_0 j_c^s = -\frac{1}{\sqrt{g}}\partial_r\left(g_{s\varphi}B_c^s + g_{\varphi\varphi}B_c^\varphi\right), \qquad (21)$$

$$\mu_0 j_c^\varphi = \frac{1}{\sqrt{g}}\partial_r\left(g_{ss}B_c^s + g_{s\varphi}B_c^\varphi\right), \qquad (22)$$

for the contravariant components of the magnetic field $\mathbf{B}_c$ and the current density $\mathbf{j}_c$. Conservation of the current is given by:

$$0 = \partial_r(\sqrt{g}j_c^r) + \partial_s(\sqrt{g}j_c^s) + \partial_\varphi(\sqrt{g}j_c^\varphi), \qquad (23)$$

where we now allow for non-zero radial current j_c^r. We only attempt to describe a solution within the fixed volume $r \leq 1$ and we assume that there is an arbitrary shielding current so that $\mathbf{B}_c$ vanishes outside of our flux rope volume.

Without loss of generality we assume that there exists a point $\gamma(s_0)$ so that $\kappa(s_0) = \tau(s_0) = 0$ and that all related derivatives also vanish. This point does not necessarily need to exist but serves as a useful point of reference. We additionally make the assumption that our magnetic field exhibits azimuthal symmetry at $\gamma(s_0)$ so that the Maxwell equations simplify to those given by Eqs. (12-14) in NC18 for a circular

cross-section. The solution for $\gamma(s_0)$ can be written as:

$$B_c^s\big|_{s=s_0} = \frac{1}{l(s)}\left(B_c^s\big|_{r=0} + \mu_0\sigma^2 \int_0^r dr'\, r'\, j_c^\varphi\big|_{s=s_0}\right), \qquad (24)$$

$$B_c^\varphi\big|_{s=s_0} = -\frac{\mu_0 l(s)}{r^2}\int_0^r dr'\, r'\, j_c^s\big|_{s=s_0}, \qquad (25)$$

where this result is slightly modified as we need to account for the parameters $l(s)$ and σ. The central magnetic field strength $B_c^s\big|_{r=0}$ appears as an integration constant that is independant of the current.

In NC18 the equations for the magnetic field were resolved by describing the current in terms of a radial power series. For our model we will alternatively use a decomposition based on shifted Legendre polynomials as it can be shown that they have certain beneficial properties for our purposes. We write the axial and poloidal current as:

$$j^s\big|_{s=s_0} = l(s) j_c^s\big|_{s=s_0} = \sum_{m=0}^\infty \beta_m \frac{1}{r}\partial_r\left(r^2 \tilde{P}_m(r)\right), \qquad (26)$$

$$j^\varphi\big|_{s=s_0} = r\sigma j_c^\varphi\big|_{s=s_0} = -\sum_{n=1}^\infty \alpha_n\, \partial_r \tilde{P}_n(r), \qquad (27)$$

where $\tilde{P}_i(r) = P_i(2r-1)$ are the shifted Legendre polynomials of i-th order that are defined for $r \in [0,1]$. In contrast to NC18 the minimum value for the n-index now stems from the fact that $\partial_r P_0(r) = 0$.

Evaluating the integrals in Eqs. (24-25) the magnetic field components then take the form:

$$\begin{aligned}
B_c^s\big|_{s=s_0} &= \frac{1}{l(s)}\left[B_c^s\big|_{r=0} - \mu_0\sigma\sum_{n=1}^\infty \alpha_n\left(\tilde{P}_n(r) - \tilde{P}_n(0)\right)\right] \\
&= \underbrace{\frac{1}{l(s)}B_c^s\big|_{r=0} + \frac{\mu_0\sigma}{l(s)}\sum_{n=1}^\infty \alpha_n\tilde{P}_n(0)}_{=-\mu_0\sigma\alpha_0\tilde{P}_0(r)/l(s)} - \frac{\mu_0\sigma}{l(s)}\sum_{n=1}^\infty \alpha_n\tilde{P}_n(r) \\
&= -\frac{\mu_0\sigma}{l(s)}\sum_{n=0}^\infty \alpha_n\tilde{P}_n(r),
\end{aligned}$$
$$(28)$$

$$B_c^\varphi\big|_{s=s_0} = -\mu_0\sum_{m=0}^\infty \beta_m\tilde{P}_m(r), \qquad (29)$$

where we additionally introduce the α_0 coefficient for $\tilde{P}_0(r) = 1$ to further simplify the expression and replace the $B_c^s\big|_{r=0}$ parameter.

We continue by making the following ansatz for the general form of the axial magnetic field component:

$$B_c^s = A_s(r,s,\varphi)B_c^s\big|_{s=s_0}, \qquad (30)$$

where A_s is an auxiliary function that fully encapsulates the axial and angular dependency of the general expression. We can easily solve for A_s in the toroidal case with constant curvature $\kappa(s) = \kappa$, zero torsion $\tau(s) = 0$ and no radial current $j_c^r = 0$. For this scenario the Eq. (20) reduces to:

$$0 = \frac{1}{\sqrt{g}}\partial_\varphi\left(g_{ss}\big|_{\substack{\kappa(s)=\kappa\\\tau(s)=0}}A_s\big|_{\substack{\kappa(s)=\kappa\\\tau(s)=0}}\right)B_c^s \qquad (31)$$

for which we find that $A_s\big|_{\substack{\kappa(s)=\kappa\\\tau(s)=0}} = C(r,s)\left[1 + r\sigma\kappa(s)\cos(\varphi)\right]^{-2}$. The integration constant $C(r,s)$ for this particular solution can be found by demanding conservation of the axial flux Φ^s for any constant value of $\kappa(s)$ with the same arrangement of coefficients. Due to the lack of any radial magnetic field component the axial flux must not only be conserved over the entirety of the cross section but also for each radial element $\partial_r\Phi^s$. We first compute the flux in the cylindrical case $\partial_r\Phi^s\big|_{s=s_0}$ which must be equal to the toroidal expression for $\partial_r\Phi^s$ from which we can directly infer $C(r,s)$:

$$\begin{aligned}
\partial_r\Phi^s\big|_{s=s_0} &= \int_0^{2\pi} d\varphi\, \sqrt{g}B_c^s\big|_{s=s_0} = 2\pi r\sigma^2 l(s)B_c^s\big|_{s=s_0} \\
&= \partial_r\Phi^s = \int_0^{2\pi} d\varphi\, \frac{C(r,s)\sqrt{g}\,B_c^s\big|_{s=s_0}}{\left[1 + r\sigma\kappa(s)\cos(\varphi)\right]^2} \\
&= \frac{2\pi r\sigma^2\, C(r,s)\, l(s)B_c^s\big|_{s=s_0}}{\sqrt{1 - r^2\sigma^2\kappa^2(s)}} \\
&\implies C(r,s) = \sqrt{1 - r^2\sigma^2\kappa^2(s)} \\
&\implies A_s\big|_{\substack{\kappa(s)=\kappa\\\tau(s)=0}} = \frac{\sqrt{1 - r^2\sigma^2\kappa^2(s)}}{\left[1 + r\sigma\kappa(s)\cos(\varphi)\right]^2}
\end{aligned}$$
$$(32)$$

Given our solution for the axial field in the cylindrical or toroidal case we can now note that $\sqrt{g}$ only depends on the curvature. As such our previously derived expression for A_s conserves the axial flux regardless of how the flux rope is curved or twisted. We can thus use the existing toroidal expression for the axial magnetic field for the general case and assume that the poloidal field and the current conform so that the Maxwell equations are resolved. Note that this does not only apply for our given A_s and one can in fact find a generalized solution with more complexity by modifying the axial field under the constraint of invariant total axial flux.

Applying this assumption to Eq. (19) and further assuming that $B_c^\varphi = A_\varphi\, B_c^\varphi\big|_{s=s_0}$ we can directly reconstruct the poloidal field. Our final combined result for both components is then given as:

$$B_c^s = -\frac{\mu_0\sigma\sqrt{1 - r^2\sigma^2\kappa^2(s)}}{l(s)\left[1 + r\sigma\kappa(s)\cos(\varphi)\right]^2}\sum_{n=0}^\infty \alpha_n\tilde{P}_n(r), \qquad (33)$$

$$\begin{aligned}
B_c^\varphi = &-\frac{\mu_0}{1 + r\sigma\kappa(s)\cos(\varphi)}\sum_{m=0}^\infty \beta_m\tilde{P}_m(r) \\
&-\frac{\mu_0 r\sigma^2\sin(\varphi)\partial_s\kappa(s)}{l(s)\left[1 + r\sigma\kappa(s)\cos(\varphi)\right]^2\sqrt{1 - r^2\sigma^2\kappa^2(s)}}\sum_{n=0}^\infty \alpha_n\tilde{P}_n(r),
\end{aligned}$$
$$(34)$$

where we now additionally find a mixture term in the poloidal field that depends on the poloidal current. The dependency of the magnetic field on the torsion $\tau(s)$ is hidden within the ϵ_s basis vector and does not explicitly appear in the expressions themselves. It is important to remember that any "axial" quantity technically includes a poloidal component when the torsion is non-zero due to our non-orthogonal coordinate system. In order to better to understand the structure of this magnetic field solution we can rewrite the solution as $\mathbf{B} = l(s)\left[1 + r\sigma\kappa(s)\cos(\varphi)\right] B_c^s \cdot \mathbf{t}(s) + B^p \cdot \hat{\epsilon}_\varphi$ so that:

$$
\begin{aligned}
B^p = {} & -\frac{\mu_0 r\sigma}{1 + r\sigma\kappa(s)\cos(\varphi)} \sum_{m=0}^{\infty} \beta_m \tilde{P}_m(r) \\
& - \frac{\mu_0 r^2 \sigma^3 \sin(\varphi)\partial_s\kappa(s)}{l(s)\left[1 + r\sigma\kappa(s)\cos(\varphi)\right]^2 \sqrt{1 - r^2\sigma^2\kappa^2(s)}} \sum_{n=0}^{\infty} \alpha_n \tilde{P}_n(r) \\
& - \frac{\mu_0 r\sigma^2 \sqrt{1 - r^2\sigma^2\kappa^2(s)}\tau(s)}{\left[1 + r\sigma\kappa(s)\cos(\varphi)\right]^2} \sum_{n=0}^{\infty} \alpha_n \tilde{P}_n(r),
\end{aligned}
$$
$$(35)$$

where we now can see the explicit dependence on the torsion.

Despite us previously claiming that any terms for $l(s)$ must drop out in physical quantities as they depend on the choice for parametrization it can be easily seen that this does not appear to be the case in Eq. (34) when additionally accounting for the scale factors. This is due to how derivatives transform under a change of parametrization $\partial_u V/l(u) \longrightarrow \partial_s V/l(s)$. As this can be a source of confusion we will from now on assume that we use an arc-length parametrized curve so that $l(s) = 1$ and drop the term from all further calculations.

By construction the current conservation in Eq. (23) is always fulfilled as long as the current is physical. This may not be the case due to singularities in the current which, due to our chosen description, can only appear at the center of the flux rope structure. An example is the poloidal current $j^\varphi\big|_{s=s_0}$ which must vanish at $r = 0$. This condition can be shown to be equivalent to:

$$
\sum_{n=1}^{\infty} \alpha_n \left(\partial_r \tilde{P}_n(r)\right)\bigg|_{r=0} = \sum_{n=1}^{\infty} (-1)^{n+1} (n^2 + n)\,\alpha_n = 0. \quad (36)
$$

which sets a constraint on the values for α_n. No such constraint exists for the β_m coefficients as j^s can take non-zero values at $r = 0$.

2.2.1. *Current Density*

By resolving Eqs. (20-22) we could generate the expressions for the current density components in our curved flux rope model. Unfortunately these expressions do not have an easily tractable form and it is very hard to extract general statements on their structure or infer any properties. We instead observe the total amount of current that flows through the flux rope that we denote as J_s:

$$
\begin{aligned}
J_s &= \int_0^1 \int_0^{2\pi} dr\, d\varphi\; \sqrt{g}\, j_c^s \\
&= \frac{2\pi\sigma^2 \sum_{m=0}^{\infty} \beta_m}{\sqrt{1 - \sigma^2\kappa^2(s)}} + \frac{2\pi\sigma^3\tau(s) \sum_{n=0}^{\infty} \alpha_n}{1 - \sigma^2\kappa^2(s)}
\end{aligned}
$$
$$(37)$$

where we find that J_s is now dependant on the curvature and the torsion. In contrast to the magnetic flux the total axial current is not invariant over the flux rope structure and sections with larger curvature posses a larger axial current. We can similarly compute the net in flowing radial current, denoted J_r, as:

$$
\begin{aligned}
J_r &= \int_0^{2\pi} d\varphi\; \sqrt{g}\; j_c^r \bigg|_{r=1} \\
&= -\frac{2\pi\sigma^4\kappa(s)\partial_s\kappa(s)\sqrt{1 - \sigma^2\kappa(s)^2}}{\left[1 - \sigma^2\kappa(s)^2\right]^2} \sum_{m=0}^{\infty} \beta_m \\
&\quad - \left(\frac{2\pi\sigma^3\partial_s\tau(s)}{1 - \sigma^2\kappa(s)^2} + \frac{4\pi\sigma^5\kappa(s)\tau(s)\partial_s\kappa(s)}{\left[1 - \sigma^2\kappa(s)^2\right]^2}\right) \sum_{n=0}^{\infty} \alpha_n.
\end{aligned}
$$
$$(38)$$

It can now be shown that the following Equation holds:

$$
\partial_s J_s + J_r = 0 \quad (39)
$$

which describes a form of current conservation. It shows that there is a non-zero net radial current which feeds the changes in axial current that arise due to changes in the curvature or torsion. Our model thus also sets strong implicit constraints on the external structure of the flux rope which must be able to provide this additional current which could become relatively large depending on the maximal values of curvature or torsion.

2.2.2. *Magnetic Fluxes*

The next physical quantity of high interest that we can derive are the magnetic fluxes. We start with the axial magnetic flux which is relatively easy as it is already partially used in the construction of our magnetic field model. We can directly compute:

$$
\begin{aligned}
\Phi^s &= \int_0^1 \int_0^{2\pi} dr\, d\varphi\, B_c^s \sqrt{g} = -2\pi\mu_0\sigma^3 \sum_{n=0}^{\infty} \alpha_n \int_0^1 dr\, r\tilde{P}_n(r) \\
&= -\pi\mu_0\sigma^3 \left(\alpha_0 + \frac{\alpha_1}{3}\right),
\end{aligned}
$$
$$(40)$$

as the integrals over the Legendre polynomials with index $n \geq 2$ vanish. The axial flux is only dependant on two parameters, namely α_0 and α_1. Due to our definition of α_0 there is a hidden interdependency with respect to all other coefficients, the relevance of which depends on how the model is configured.

For the poloidal flux, in a well behaved Frenet-Serret frame, we can show that:

$$\Phi^\varphi = \int_0^1 \int_0^{s_{\max}} dr\, ds\, B_c^\varphi \sqrt{g} = -L\mu_0\sigma^2 \left(\frac{\beta_0}{2} + \frac{\beta_1}{6}\right)$$
$$- \mu_0\sigma^4 \sin(\varphi) \underbrace{\int_0^1 \int_0^{s_{\max}} dr\, ds\, \frac{r^2 \partial_s\kappa(s)}{[\ldots]\,\sqrt{\cdots}} \sum_{n=0}^{\infty} \alpha_n \tilde{P}_n(r)}_{= 0 \text{ if } \kappa(0)=\kappa(s_{\max})},$$
(41)

where L is the total length of the flux rope and the second integral term vanishes automatically if the flux rope is closed (for proof see A). Again the total poloidal flux is only determined by the first two coefficients of the axial current. Specifically the poloidal flux also independant of the curvature of the flux rope and scales linearly with the flux rope length L.

2.2.3. *Magnetic Energy*

The total magnetic energy stored within the flux rope is given by the following integral:

$$E = \int_0^1 \int_0^{s_{\max}} \int_0^{2\pi} \frac{g_{ij}B_c^i B_c^j}{2\mu_0} \sqrt{g}\, dr\, ds\, d\varphi, \qquad (42)$$

which is hard to analytically calculate as it involves integrals over triple Legendre polynomials. The expression for the magnetic energy density:

$$g_{ij}B_c^i B_c^j = g_{ss}\left(B_c^s\right)^2 + g_{\varphi\varphi}\left(B_c^\varphi\right)^2 + g_{s\varphi}B_c^s B_c^\varphi \qquad (43)$$

consists of three different terms where the first two always have a positive sign. The third term on the other hand depends on the sign of the torsion $\tau(s)$ and the sign of $B_c^s B_c^\varphi$ which depends on the handedness of the magnetic field. While more hidden, the magnitude of $\left(B_c^\varphi\right)^2$ also depends the handedness of the field due to the second term in the poloidal expression. As such the magnetic energy density is generally split into two separate energy levels whenever there is non-zero torsion or changing curvature. For the general representation we will introduce the following integral:

$$_k\mathcal{E}_{nm}^l = \int_0^1 dr\, r^k \tilde{P}_n(r)\tilde{P}_m(r)\left[1 - r^2\sigma^2\kappa^2(s)\right]^l, \qquad (44)$$

where higher orders in k, n or m will lead to asymptotically smaller values in dependence of the curvature. The total magnetic energy, making use of summation over double indices, can then be written as:

$$E = \pi\sigma^4\mu_0 \int_0^{s_{\max}} ds \left(_1\mathcal{E}_{nn'}^1 \alpha_n\alpha_{n'} + {}_3\mathcal{E}_{mm'}^{-1}\beta_m\beta_{m'}\right.$$
$$+ \sigma^2\tau^2(s)\, _3\mathcal{E}_{nn'}^{-\frac{3}{2}}\alpha_n\alpha_{n'} + \frac{\sigma^4\kappa^2(s)\tau^2(s)}{2}\, _5\mathcal{E}_{nn'}^{-\frac{3}{2}}\alpha_n\alpha_{n'} \quad (45)$$
$$\left. + \frac{\sigma^4\left[\partial_s\kappa(s)\right]^2}{2}\, _5\mathcal{E}_{nn'}^{-\frac{5}{2}}\alpha_n\alpha_{n'} + 2\sigma\tau(s)\, _3\mathcal{E}_{nm}^{-1}\alpha_n\beta_m\right)$$

where the last term represents the energy splitting. Note that the terms that depend on the change of the curvature cancel out when integrating over the entire cross-section so that only the axial integral over the torsion produces a difference in energy due to the handedness.

2.3. *Lorentz Forces*

The last property of our model that we will analytically explore are the arising Lorentz forces. The three contravariant components of the Lorentz force can be calculated using the same Equations from Eq. (29) in NC18:

$$F_c^r = g^{rr} \sqrt{g}\left(j_c^s B_c^\varphi - j_c^\varphi B_c^s\right) \qquad (46)$$

$$F_c^s = \sqrt{g}\left(g^{s\varphi} j_c^r B_c^s - g^{ss} j_c^r B_c^\varphi\right) \qquad (47)$$

$$F_c^\varphi = \sqrt{g}\left(g^{\varphi\varphi} j_c^r B_c^s - g^{s\varphi} j_c^r B_c^\varphi\right) \qquad (48)$$

where now in general all three values will be non-zero as there is a radial current. Nonetheless the typical arising radial currents will be comparatively small and the radial Lorentz force can be expected to be the dominant component. The expressions for these forces will be of similar complexity to those of the current and it is therefore not practical to show their full form. Alternatively we can attempt to compute the net radial force that acts on a slice of our flux rope using:

$$F_R = <F^r> = \int_0^1 \int_0^{2\pi} dr\, d\varphi\, \sqrt{g}\epsilon_r F_c^r. \qquad (49)$$

In order to further simplify this quantity we expand our result to third order in curvature (first order for derivatives), first order in torsion and only consider the first two coefficients (α_0, β_0). For a torus-like geometry the net force acting on the cross-section can then be evaluated as:

$$F_R\big|_{\substack{\kappa(s)=\kappa \\ \tau(s)=0}} \approx \frac{\pi}{8}\mu_0\sigma^4\kappa(s)\left[\sigma^2\left(2\alpha_0^2 - 5\beta_0^2\right)\kappa^2(s) - 6\beta_0^2\right] \cdot \mathbf{n}(s),$$
(50)

which we find to act fully along the direction defined by the normal vector $\mathbf{n}(s)$. The first term α_0^2 points inwards and thus acts as the tension force with the other two terms given by β_0^2 pointing outwards and thus representing the magnetic hoop force. For the more general form we can investigate any forces acting along the binormal vector $\mathbf{b}(s)$ using the same approximations and allowing for changes in curvature:

$$\mathbf{b}(s) \cdot F_R \approx \frac{\pi}{12}\alpha_0\mu_0\sigma^5\partial_s\kappa(s)\left(\sigma^2\kappa^2(s)\left[19\beta_0 + 23\alpha_0\sigma\tau(s)\right]\right.$$
$$\left. + 15\left[\beta_0 + \alpha_0\sigma\tau(s)\right]\right).$$
(51)

The conclusion of this result is that the flux rope will twist around itself if there is any change in curvature which can lead to instability. As this force contains terms of $\alpha_0\beta_0$ it

is also dependent on the handedness of the magnetic field. The Lorentz forces that are generated by our model thus lead to rather complicated dynamics which would require simulations to fully analyze. Such simulations could give hints on the stability or the instability of a selected flux rope geometry or a specific magnetic field configuration.

2.4. *Configuration of Coefficients*

We will now briefly discuss how we can configure the current coefficients α_i and β_i so that the resulting model exhibits certain properties. As our coefficients are defined for a point on the flux rope that is cylindrical it also makes sense to configure the model at our point of reference s_0. We start by defining an arbitrary radial twist function $Q(r)$ and demand that:

$$Q(r) = \sum_{l=0}^{\infty} \gamma_l \tilde{P}_l(r) = \frac{B^\varphi}{rB^s} = \frac{h_\varphi B_c^\varphi}{rh_s B_c^s} = \frac{\sum_{m=0}^{\infty} \beta_m \tilde{P}_m(r)}{\sum_{n=0}^{\infty} \alpha_n \tilde{P}_n(r)}, \quad (52)$$

where γ_l are the coefficients for an expansion, using shifted Legendre polynomials, of our prescribed twist distribution function. Using the following two properties for shifted Legendre polynomials:

$$\int_0^1 \tilde{P}_m(r)\tilde{P}_n(r) = \frac{\delta_{nm}}{2m+1} \quad (53)$$

$$\int_0^1 dr\, \tilde{P}_{m+n-2k}(r)\tilde{P}_m(r)\tilde{P}_n(r) = \frac{1/2}{2m+2n-2k+1} \frac{\lambda_k \lambda_{m-k}\lambda_{n-k}}{\lambda_{m+n-k}},$$
$$\lambda_k = \frac{(2k)!}{2^k(k!)^2}, \quad (54)$$

where a derivation for the integral over the triple product is given in Dougall (1953), we can rearrange Eq. (52) and solve for β_m so that:

$$\beta_m = (2m+1) \int_0^1 dr\, \tilde{P}_m(r)\left(\sum_{l=0}^{\infty} \gamma_l \tilde{P}_l(r)\right)\left(\sum_{n=0}^{\infty} \alpha_n \tilde{P}_n(r)\right)$$
$$= (2m+1) \sum_{n=0}^{\infty} \sum_{k=0}^{\min(m,n)} \frac{\alpha_n \gamma_{n+m-2k}}{2m+2n-2k+1} \frac{\lambda_k \lambda_{m-k}\lambda_{n-k}}{\lambda_{m+n-k}}. \quad (55)$$

From this expression we see that we can describe any arbitrary twist distribution for any arbitrary set of coefficients α_n. We are thus able to halve the degrees of freedom by setting a fixed twist distribution.

In order to determine the α_i coefficients we require a second constraint for which we can use the radial Lorentz force:

$$\mu_0^{-1} F_c^r\Big|_{s=s_0} = -2r\tilde{P}_m(r)\tilde{P}_{m'}(r)\beta_m\beta_{m'} + 2r^2 \tilde{P}_n(r)\tilde{P}_m(r)\alpha_n\beta_m$$
$$+ 2\tilde{P}_n(r)\tilde{P}_{n'}(r)\alpha_n\alpha_{n'}. \quad (56)$$

In theory one could repeat the same process as with $Q(r)$ for F_c^r but this turns out to be significantly more complicated and requires the evaluation of integrals over four Legendre polynomials. In practice it is easier to minimize F_c^r for a fixed number of coefficients.

In the remaining parts of our paper we will exclusively make use a uniform twist and nearly force-free configuration which can be defined in a more direct way and does not require us to explicitly solve for a vanishing radial Lorentz force.

3. MODEL EXAMPLE

We will now show a specific implementation of our model in terms of a purely analytically defined flux rope geometry. We use an open parametrized path of the form:

$$\gamma(s) = \left\{\left(1 - \frac{s}{2}\right)\sin(3\pi s), \left(\left(1 - \frac{s}{2}\right)\sin(2\pi s), \frac{1 + \sin^2(\frac{\pi s}{2})}{2\pi}\right\}\right\}, \quad (57)$$

for the range $s \in [0, 1]$. The parametrization of this helix-like path was specifically chosen so that the curvature does not completely or nearly vanish at any position. This guarantees that we do not have any issues constructing a Frenet-Serret frame at any point along the path as the construction can also additionally be numerically unstable for small curvature values. Regarding other model parameters we set $\sigma = 0.1\,AU$ and $B^s\big|_{s=s_0} = 15\,nT$ which serve as typical parameters for an ICME at $1\,AU$.

3.1. *Uniform Twist Force-Free Configuration*

As previously mentioned we will make use of a uniformly twisted magnetic field configuration where we additionally chose the coefficients so that the flux rope is force-free for a cylindrical geometry. From previous calculations it easy to verify that for a uniformly twisted flux rope $\beta_i = \gamma_0 \alpha_i$ for all indices i. We determine the α_i coefficients by using the analytical solution for the Gold-Hoyle model (Gold & Hoyle 1960):

$$\alpha_i = \int_0^1 dr\, \frac{B_c^s\big|_{r=0}}{1 + \gamma_0^2 r^2}. \quad (58)$$

The number of coefficients that are required to deliver sufficient accuracy to approximate the Gold-Hoyle solution depends on the twist parameter γ_0 with a higher twist requiring higher order coefficients. Normally only few coefficients are needed for a good approximation of the magnetic field but significantly higher orders are required for accurately depicting the current (and therefore also the Lorentz forces). There also exists an optimal or maximum order beyond which the approximation will begin to diverge that is also further dependent on the twist. For our purposes we will use a dozen
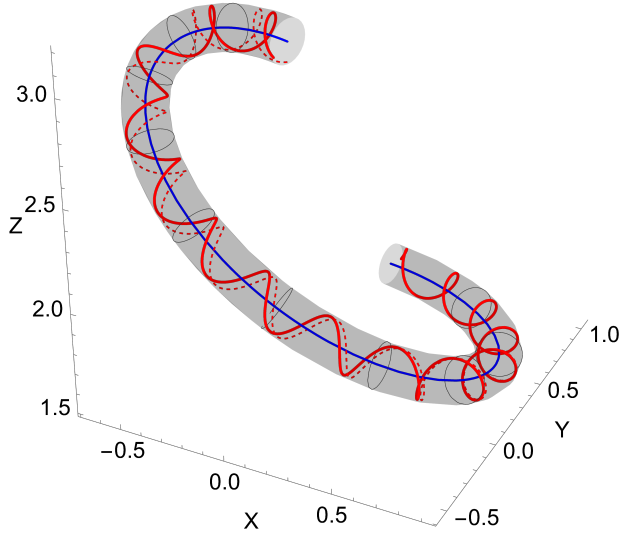
Figure 2. Exemplary flux rope structure given by Eq. (57). The blue central line follows the parametrized path $\boldsymbol{\gamma}(s)$ and the two red line are integrated magnetic field lines. The solid red field line gives the physical solution according to our results in Eqs. (33 & 34) while the dashed red field line is based on a toroidal approximation which does not take account for effects of changing curvature or torsion. Both field lines start at the same position $(r, s, \varphi) = (0.95, 0.0, 0.0)$ and the twist is set to $\gamma_0 = 2$. The position $s = 0$ corresponds to the bottom and $s = 1$ to the top.

coefficients in order to deliver sufficient accuracy for the current and the derived Lorentz forces.

It is at this point that we would also like to highlight why we have chosen our particular approach with the more complicated Legendre polynomials instead of using a radial power series expansion. A Taylor expansion of the Gold-Hoyle solution takes the following form:

$$\frac{1}{1 + \gamma_0^2 r^2} = 1 - \gamma_0^2 r^2 + \gamma_0^4 r^4 - \gamma_0^6 r^6 + \gamma_0^8 r^8 \dots \quad (59)$$

where it is immediately apparent that the power series diverges for any twist values $\gamma_0 \geq 1$. The models described in NC16/NC18 are thus incapable of describing all uniform twist configurations even with an unlimited number of coefficients. These issues are bypassed by using a description in terms of Legendre polynomials although other, less severe, pitfalls may appear.

3.2. *Visualization*

Figure 2 shows the exemplary flux rope structure given by Eq. (57) with the parametrized curve $\boldsymbol{\gamma}(s)$ highlighted in blue. The path initially ($s \approx 0$) resembles a helix with near constant curvature and torsion and the curvature increases over the axis reaching a maximum near the end ($s \approx 0.8$).

We further plotted two integrated magnetic field lines (red) which show the twisting of the magnetic field within this structure. The first field line, in solid red, shows the magnetic field line of our derived model with a constant twist of $\gamma_0 = 2$. The second field line, dashed red, shows a magnetic field line of the same twist but as a toroidal approximation. This allows us to visually compare our model solution with classical toroidal solutions and compare the effects on the twisting of the field lines. From our example here we see that the local twist along the axis changes significantly and that our generally curved solution exhibits lower twist than the toroidal approximation. As we will see later this change in twist does not only change over the axis but also varies across the entire cross-section. As a consequence this also shows that is significantly harder to estimate flux rope twist values as they will locally vary from just deformations of the geometry.
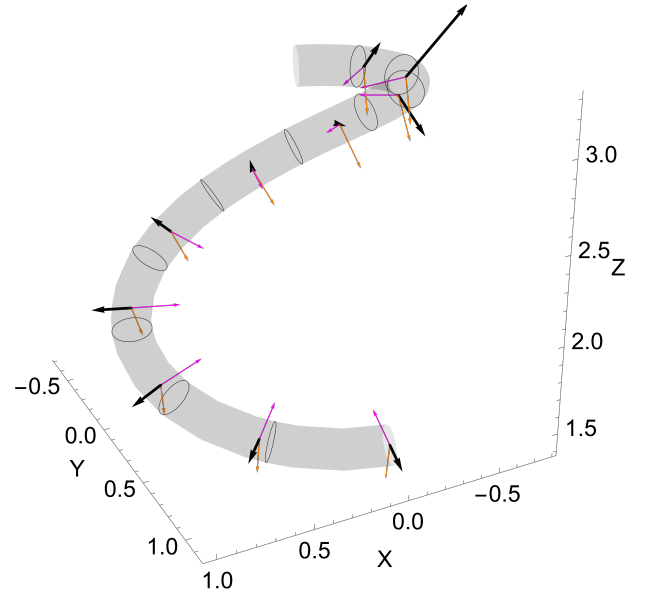

Figure 3. Exemplary flux rope structure with net Lorentz force vectors that are defined for all three components similarly to Eq. (49) at ten equidistant, in terms of the parameter s, positions along the flux rope. The local normal vectors $\boldsymbol{n}(s)$ (magenta) and the binormal vectors $\boldsymbol{b}(s)$ (orange) are shown at these same positions for reference. For a toroidal or nearly toroidal geometry the net Force acting on the cross-section is the hoop force along the inverse normal vector (e.g. bottom). At other positions (e.g. top) when the flux rope becomes highly twisted the net force can also act in other directions leading to a complicated time-evolution of the overall structure.

Figure 4 shows 12 panels for the absolute magnetic field strength B, the absolute current density J, local twist Q and the $\mathbf{J} \times \mathbf{B}$ misalignment at three varying positions along our flux rope. The cross-sections are arranged so that $x = -1$
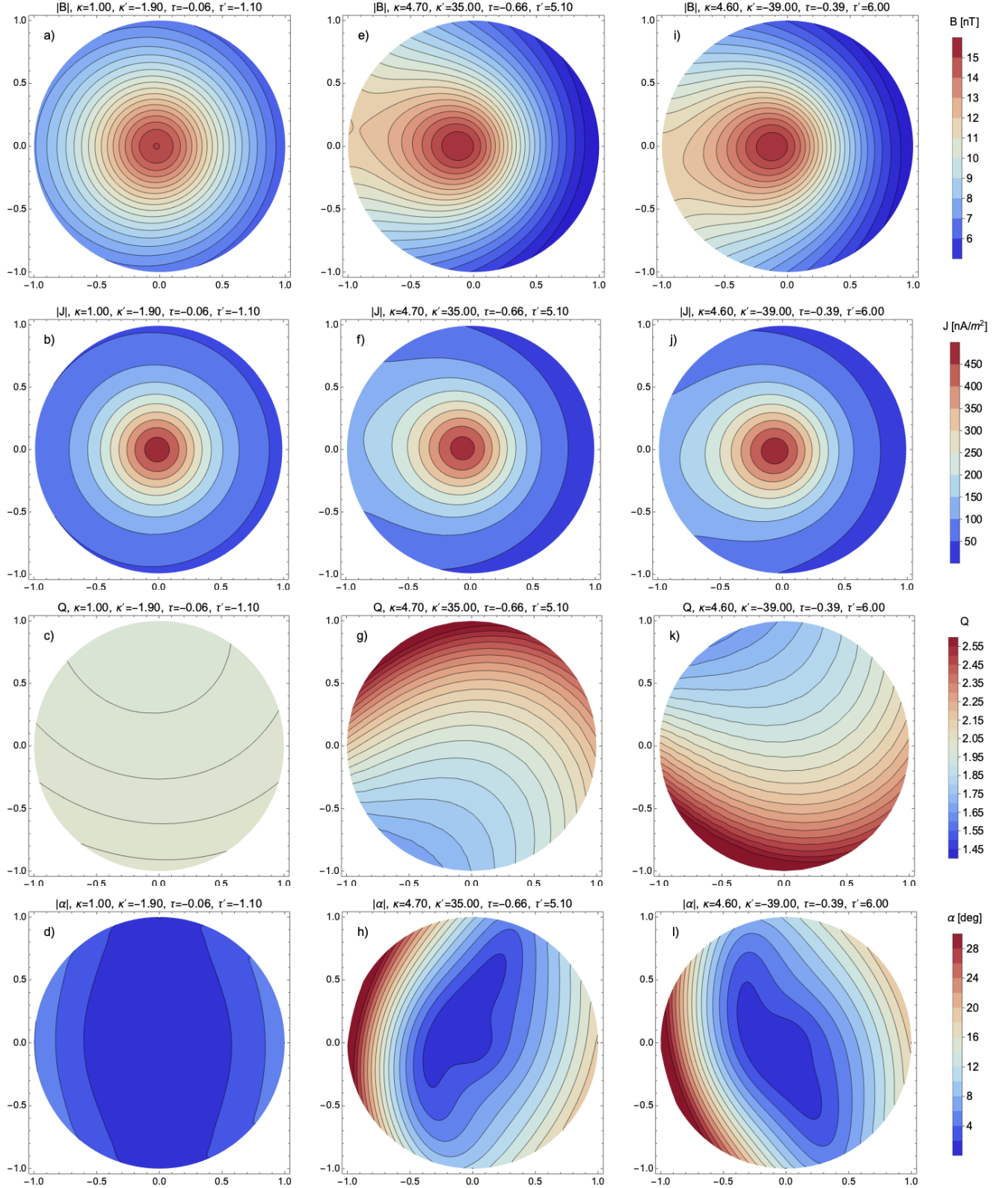
Figure 4. Three different magnetic field B, current density J, twist Q and $\mathbf{J} \times \mathbf{B}$ misalignment cross-section contour plots for the flux rope given by Eq. (57) at the positions $s = 0$ (left), $s = 0.75$ (center) and $s = 0.8$ (right). The position $x = -1$ corresponds to the most inner part of the flux rope ($\varphi = \pi$), $x = +1$ the most outer part ($\varphi = 0$) and $y = \pm 1$ down and up respectively. The left column corresponds to a nearly toroidal geometry and the middle/right columns represent strongly twisted geometries with increasing or decreasing curvature. The effect of changing curvature and torsions appears to rotate the magnetic field and current profiles while having strongly asymmetric effects on the local magnetic twist and $\mathbf{J} \times \mathbf{B}$ misalignment.

corresponds to the most inner part of the flux rope ($\varphi = \pi$), $x = +1$ the most outer part ($\varphi = 0$) and $y = \pm1$ down and up respectively. The sign of the y-axis appears inverted because the binormal vector $\mathbf{b}(s)$ generally points towards the negative 3D Z-axis in our example.

The first column (a-d), for which $s = 0$, represents the nearly toroidal section of our flux rope. At this point we see that the structure of our magnetic field and the current exhibits a small backwards shift. The local twist remains nearly constant over the entirety of the cross-section and it is also mainly force-free with only small misalignment's at the back and front of the structure. These results are very similar to those shown in (Vandas & Romashets 2017a) which uses a toroidal geometry and a uniformly twisted magnetic field and are therefore expected to be essentially the same.

The middle (e-h) and right (i-l) columns represent two strongly twisted sections of the flux rope with inverted signs for the change of curvature. The magnetic field and current density contour plots show a stronger shift due to the higher curvature values but additionally appear to be rotated. The direction of this rotation depends on the sign of the change in curvature, the sign of the torsion and the handedness of the magnetic field. The panels (g) & (k) show strongly distorted twist profile with significant local deviations in the twist number of up to ±0.5. Despite the appearance of a rough balance for the size of the higher and lower twist regions the field line in our example exhibits lower twist. This is due to the fact that a field line will azimuthally rotate faster when experiencing a higher twist which leads it to occupy the lower twist region for longer. Lastly the panels (h) & (l) show to strongly distorted profiles for the $\mathbf{J} \times \mathbf{B}$ misalignment. In both cases the flux rope core remains largely force-free but with large forces arising specifically at the back of structure and weaker forces at the front. These profiles are also rotated similarly to the magnetic field and the current with the rotation angle appearing to be larger. While it is not shown in this contour plot these forces generally act towards the $x = +1$ so that, in the absence of external forces, the entire flux rope geometry will expand over time.

The Lorentz forces are shown in more detail in Figure 3 where we show the resulting net Lorentz forces, in black, according to Eq. (50) which we compute numerically for our example instead of using the simpler approximations. For comparison this figure also includes the normal (magenta) and binormal (orange) Frenet-Serret vectors. For sections of the flux rope that are nearly toroidal ($s \approx 0$) we can see that the net force mainly consists of the hoop force and also acts along that direction (inverse of $\mathbf{n}$). For more twisted section we start to see that the net force does not act along the same direction as the hoop force, specifically towards the top/end of our example. We can see that the net force can contain a large binormal component and seemingly acts in a random

direction. Our model thus exhibits rather complicated dynamics which would require simulations to fully analyze.

3.3. *Synthetic Magnetic Field Profiles*

While the previously shown global visualizations can further the understanding of our flux rope model they cannot be directly verified or measured. We therefore additionally turn to synthetic in-situ magnetic field profiles as generated by virtual spacecraft trajectories in order to generate synthetic measurements that could be compared to real data.
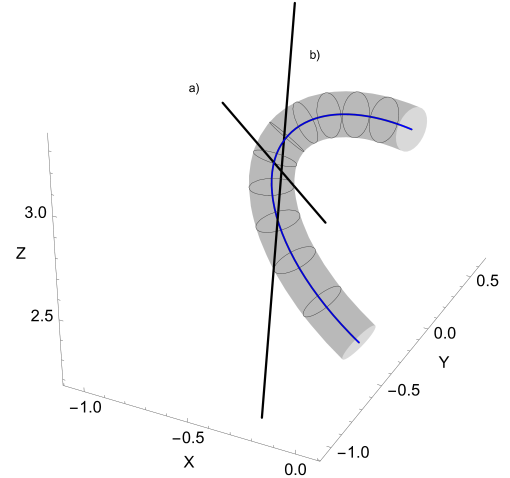

Figure 5. A small cut out of the upper section of our flux rope example including two virtual spacecraft trajectories. The first trajectory, marked as (a), represents a classical frontal impact of an ICME. The second trajectory, marked as (b), implicates a pass through an ICME flank without an exit to the inside of the flux rope.

Figure 5 shows the two virtual spacecraft trajectories which we will use for our examples. The first virtual trajectory, denoted as (a), represents a classical magnetic flux rope measurement. In the second case, where the trajectory is denoted as (b), the spacecraft traverses through a large portion of the flux rope leading to a significantly longer measurement and highly asymmetric measurement.

The resulting synthetic profiles, for both cases, are shown in Figure 6 and are plotted in terms of an arbitrary length measure along virtual trajectories. For the first case we see that the profile matches the classical case of a rotating magnetic field profile. The latter part of the synthetic measurement, which corresponds to the compressed inner volume of the curved flux rope, has a stronger absolute magnetic field strength creating a slightly asymmetric profile in terms of magnitude. Our second case is very different showing the typical magnetic field rotation at the start of the measurement then settling into a very static decaying profile as the spacecraft traverses side sways through the flux rope structure. Extreme asymmetries, for which flux rope expansion
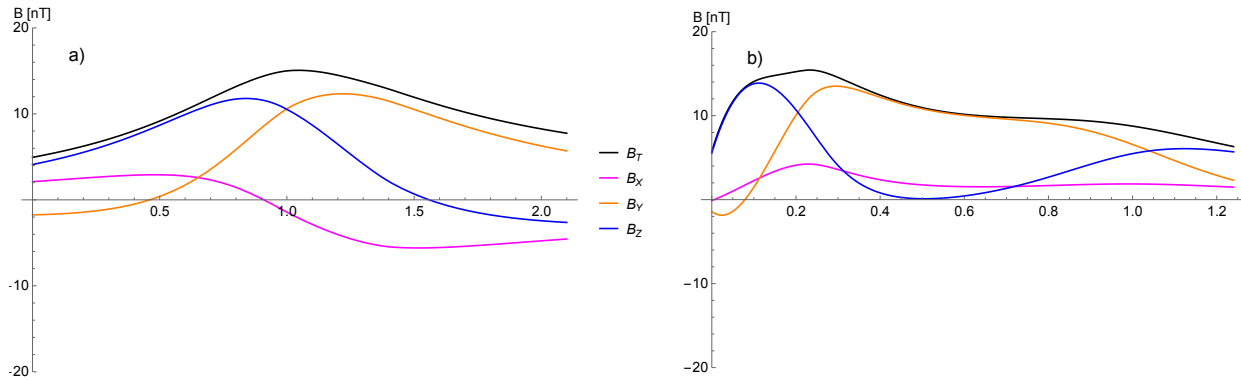
Figure 6. Two synthetic in-situ profiles generated by the virtual spacecraft trajectories given in Figure 5. The left profile (a) represents a classical frontal fly through and generated the commonly seen rotating magnetic field profile. The right profile (b) describes a flanking pass with an initially fast rotation of the magnetic field and a long largely constant tail. The x-axis corresponds to an arbitrary length parameter along the path of the trajectory.

alone cannot be the cause, can also sometimes be seen in real in-situ data and could therefore be interpreted as flank hits that are similar to our proposed scenario (Owens et al. 2012). Note that in both cases the flux rope size is fixed and that in both our synthetic measurements we do not include any effects due to expansion.

4. DISCUSSION & CONCLUSION

In this paper we have introduced the basic mathematical concepts that are necessary to describe arbitrarily curved flux rope structures under the constraint of a circular cross-section. We furthermore derived a specific solution to Maxwell equations for this geometry which requires the introduction of an implicitly defined radial current that imposes further conditions on our flux rope model that we do not investigate in detail. This raises the hope that the same can be done in the future for more complicated cross-section shapes allowing the analytical treatment of flux ropes without any inherent symmetry conditions and high flexibility. The primary issues with our current approach is the Frenet-Serret frame which is very hard to apply to general space curves due to the problems at points with vanishing curvature. Alternatives, such as those described in (Bishop 1975), exist and solve this issue but are harder to implement. For non-circular cross-section an additional degree of freedom is necessary to properly set the orientation. In most other models the flux ropes are only considered to lie within a plane which sets a natural up or down direction along which the cross-section can be orientated. This is no longer the case for general space curves and thus makes the problem more complicated.

The magnetic field solutions that we derive within this paper solve the Maxwell equations but nonetheless appear to have strange properties regarding the radial currents. The flux rope still possesses a clear magnetic boundary at its edge but the same cannot be said for the current and this implicitly sets unknown conditions on the external region that surrounds it. As was already remarked in NC18, radial currents can also be introduced into cylindrical or toroidal geometries to break azimuthal symmetry. The exact nature of such a radial current and the resulting physical implications are, at this point in time, not entirely clear to us. Additionally, it may be possible to find more consistent solutions by allowing for a varying cross-section that can be locally adapted to define a boundary through which there is no magnetic flux and no current.

With the usage of Legendre polynomials and NC16/NC18 there are now at least two approximate approaches for describing the internal magnetic field structures for the type of models that we use in this paper. For uniformly twisted fields the Legendre approach is clearly superior but it may have unknown drawbacks in other scenarios. We also have not attempted to describe the evolution of the coefficients regarding flux rope expansion which will differ depending on the polynomial basis that is used. In the future it may be necessary to more closely analyze these approaches for different scenarios. For both cases, the degrees of freedom that arise due when using many coefficients are too high to be properly analyzed in real data. It is thus clear that no matter which approach is used that there must be a simple description of the magnetic field. This can either be a uniform twist number as with the uniformly twisted field, an α parameter for a linear force-free field or another parameter for other type of distributions.

While we have only performed a purely mathematical approach our model is fairly straight forward to implement for numerical applications which will be the focus of future papers. The parametrized path $\gamma(s)$ can easily be described using splines, which must be of at least third order, which also allows for easy calculation of the curvature, torsion and the Frenet-Serret vectors. Transformation of Cartesian coordinates into our curvilinear coordinate system is fairly straightforward using minimization algorithms under the condition

that good initial starting values are used. A basic implementation for some of these procedures was required to generate the synthetic profiles shown in Fig. 6 and are contained in the notebooks on the repository linked in the acknowledgements. A spline implementation, in the future, should allow for easy time evolution if the spline points are interpreted as representative particles with mass. This should allow us to build purely analytic simulations and evolve the flux rope geometry according to the arising Lorentz forces or additional external factors such as the solar wind environment or the coronal magnetic field.

The results from Fig. 4 show highly asymmetric Lorentz force distributions when we include effects due to changing curvature or torsion. It is therefore highly likely that our usage of a circular cross-section is a strong approximation and that this shape will become additionally distorted over time. In order to test how valid this approximation is, and under which conditions it may be suitable, would require a more sophisticated numerical MHD simulations. A recent paper shows how to implement generally distorted cross-sections

using a similar framework which can be readily adopted to our model (Nieves-Chinchilla et al. 2022).

Overall we believe that this paper serves as another useful contribution, building on previous work in NC16/NC18, for extending the framework to describe complex flux rope geometries. Despite using the constraint of a circular cross-section the flexibility that is gained by describing the flux rope in terms of a general space curve allows for an extremely high variety of different configurations to be explored. While our work primarily concerns itself with ICME flux ropes this model can also be applied to flux rope structures significantly closer to the Sun or on the solar surface.

REFERENCES

Bishop, R. L. 1975, The American Mathematical Monthly, 82, 246. http://www.jstor.org/stable/2319846

Bothmer, V., & Schwenn, R. 1998, Annales Geophysicae, 16, 1, doi: 10.1007/s00585-997-0001-x

Burlaga, L., Sittler, E., Mariani, F., & Schwenn, R. 1981, J. Geophys. Res., 86, 6673, doi: 10.1029/JA086iA08p06673

Davies, E. E., Möstl, C., Owens, M. J., et al. 2021, A&A, 656, A2, doi: 10.1051/0004-6361/202040113

Démoulin, P., & Dasso, S. 2009, A&A, 498, 551, doi: 10.1051/0004-6361/200810971

Dougall, J. 1953, Proceedings of the Glasgow Mathematical Association, 1, 121–125, doi: 10.1017/S2040618500035590

Farrugia, C. J., Osherovich, V. A., & Burlaga, L. F. 1995, J. Geophys. Res., 100, 12293, doi: 10.1029/95JA00272

Gold, T., & Hoyle, F. 1960, MNRAS, 120, 89, doi: 10.1093/mnras/120.2.89

Gosling, J. T., McComas, D. J., Phillips, J. L., & Bame, S. J. 1991, J. Geophys. Res., 96, 7831, doi: 10.1029/91JA00316

Gulisano, A. M., Démoulin, P., Dasso, S., & Rodriguez, L. 2012, A&A, 543, A107, doi: 10.1051/0004-6361/201118748

Hidalgo, M. A., Nieves-Chinchilla, T., & Cid, C. 2002, Geophys. Res. Lett., 29, 1637, doi: 10.1029/2001GL013875

Hinterreiter, J., Amerstorfer, T., Temmer, M., et al. 2021, Space Weather, 19, e02836, doi: 10.1029/2021SW002836

Hu, Q., Qiu, J., & Krucker, S. 2015, Journal of Geophysical Research (Space Physics), 120, 5266, doi: 10.1002/2015JA021133

Isavnin, A. 2016, ApJ, 833, 267, doi: 10.3847/1538-4357/833/2/267

Kay, C., & Gopalswamy, N. 2018, Journal of Geophysical Research (Space Physics), 123, 7220, doi: 10.1029/2018JA025780

Kay, C., Opher, M., & Evans, R. M. 2015, ApJ, 805, 168, doi: 10.1088/0004-637X/805/2/168

Leitner, M., Farrugia, C. J., MöStl, C., et al. 2007, Journal of Geophysical Research (Space Physics), 112, A06113, doi: 10.1029/2006JA011940

Lepping, R. P., Jones, J. A., & Burlaga, L. F. 1990, J. Geophys. Res., 95, 11957, doi: 10.1029/JA095iA08p11957

Liu, Y., Richardson, J. D., Belcher, J. W., et al. 2006, Journal of Geophysical Research (Space Physics), 111, A12S03, doi: 10.1029/2006JA011890

Lugaz, N., Farrugia, C. J., Davies, J. A., et al. 2012, ApJ, 759, 68, doi: 10.1088/0004-637X/759/1/68

Lundquist, S. 1950, Ark. Fys., 2, 361. https://ci.nii.ac.jp/naid/10003639556/en/

Möstl, C., Rollett, T., Frahm, R. A., et al. 2015, Nature Communications, 6, 7135, doi: 10.1038/ncomms8135

Mulligan, T., & Russell, C. T. 2001, J. Geophys. Res., 106, 10581, doi: 10.1029/2000JA900170

Nieves-Chinchilla, T., Hidalgo, M. A., & Cremades, H. 2022, APJ submitted

Nieves-Chinchilla, T., Linton, M. G., Hidalgo, M. A., & Vourlidas, A. 2018, ApJ, 861, 139, doi: 10.3847/1538-4357/aac951

Nieves-Chinchilla, T., Linton, M. G., Hidalgo, M. A., et al. 2016, APJ, 823, 27, doi: 10.3847/0004-637X/823/1/27

Owens, M. J., Démoulin, P., Savani, N. P., Lavraud, B., & Ruffenach, A. 2012, SoPh, 278, 435, doi: 10.1007/s11207-012-9939-2

Riley, P., & Crooker, N. U. 2004, ApJ, 600, 1035, doi: 10.1086/379974

Rollett, T., Möstl, C., Temmer, M., et al. 2014, ApJL, 790, L6, doi: 10.1088/2041-8205/790/1/L6

Vandas, M., & Romashets, E. 2017a, A&A, 608, A118, doi: 10.1051/0004-6361/201731412

—. 2017b, SoPh, 292, 129, doi: 10.1007/s11207-017-1149-5

Vandas, M., Romashets, E., & Watari, S. 2005, Planet. Space Sci., 53, 19, doi: 10.1016/j.pss.2004.09.024

Vourlidas, A., Lynch, B. J., Howard, R. A., & Li, Y. 2013, SoPh, 284, 179, doi: 10.1007/s11207-012-0084-8

Weiss, A. J., Möstl, C., Amerstorfer, T., et al. 2021, ApJS, 252, 9, doi: 10.3847/1538-4365/abc9bd

APPENDIX

A. POLOIDAL FLUX INTEGRAL

We want to show that the integral:

$$\mu_0 \sigma^4 \sin(\varphi) \int_0^1 \int_0^{s_{\max}} dr \, ds \, \frac{r^2 \partial_s \kappa(s)}{[1 + r\sigma\kappa(s)\cos(\varphi)] \sqrt{1 - r^2\sigma^2\kappa^2(s)}} \sum_{n=1}^{\infty} \alpha_n \tilde{P}_n(r) = 0, \tag{A1}$$

vanishes. It can already be seen, due to the $\sin(\varphi)$ dependance, that the term must vanish as the poloidal flux must be invariant with respect to the φ parameter. We start by expanding the fraction using a Taylor series in terms of the curvature $\kappa(s)$:

$$\frac{1}{[1 + r\sigma\kappa(s)\cos(\varphi)] \sqrt{1 - r^2\sigma^2\kappa^2(s)}} = \sum_{k=0}^{\infty} a_k \kappa^k(s), \tag{A2}$$

where a_k are undefined coefficients which are not of importance. Using integration by parts we can then rewrite the integral for every k:

$$\int_0^{s_{\max}} ds \, \kappa^k(s) \partial_s \kappa(s) = \left[\kappa^k(s)\kappa(s)\right]_0^{s_{\max}} - k \int_0^{s_{\max}} ds \, \kappa^{k-1}(s) \left(\partial_s \kappa(s)\right) \kappa(s). \tag{A3}$$

Finally, using the condition that $\kappa(0) = \kappa(s_{\max})$ the first term on the right hand side vanishes and we receive:

$$\int_0^{s_{\max}} ds \, \kappa^k(s) \partial_s \kappa(s) = -k \int_0^{s_{\max}} ds \, \kappa^k(s) \partial_s \kappa(s)$$

$$\implies \int_0^{s_{\max}} ds \, \kappa^k(s) \partial_s \kappa(s) = 0, \, \forall k, \, k \geq 0, \tag{A4}$$

with which our claim has been proven.